Supersaturation and Droplet Spectral Evolution in Fog

H. GERBER*

Naval Research Laboratory, Washington, D.C.

(Manuscript received 3 December 1990, in final form 22 May 1991)

ABSTRACT

Droplet sizes, larger than expected, and transient water vapor supersaturations were measured in radiation fog. Nongradient turbulent mixing of saturated air parcels at different temperatures and the release of excess vapor by molecular diffusion at the interface between the mixing parcels are suggested as the mechanisms causing the large supersaturations. Approximate agreement is found between calculated rates of change of supersaturation during nongradient mixing and the supersaturation measurements. A stochastic mixing model, based on the supersaturation and other measurements in the fogs, is used to estimate if nongradient mixing and transient supersaturations cause the appearance of large droplets. The model predicts a broadening of the droplet spectra to include no larger than midsized droplets. This study concludes that a form of nonlocal turbulence closure may be required in models to accurately describe microphysics in fogs and clouds when nongradient mixing is important. This mixing causes droplet broadening and activation of cloud condensation nuclei within fogs and clouds; the effect is both proportional to the temperature difference of mixing saturated air parcels and inversely proportional to the droplet integral radius.

1. Introduction

The central theme of this paper is an attempt to explain large values of water vapor supersaturation, S, measured in radiation fog. The observed values of S are best summarized as being as large as several tenths of 1% in magnitude and transient in nature, lasting as long as tens of seconds. A corollary to this theme is to determine if these supersaturations cause the observed rapid evolution of the droplet spectra to larger droplet sizes.

The first direct measurements of water vapor supersaturation were made at Lake Fairfax County Park in shallow radiation fog (Gerber 1981) using the saturation hygrometer described by Gerber (1980). Measured values of S were as large as 0.5%, which, due to the use of a low-frequency filter on the output of the instrument, may still have been an underestimate of the true maxima. The hygrometer was used a second time during the 1982 Fog Project at ASRC (Atmospheric Science Research Center, State University of New York, Albany; Jiusto and Lala 1983; Meyer et al. 1986; Fitzjarrald and Lala 1989; Meyer and Lala 1990). Sufficient measurements were made to judge the practicality of the hygrometer, and again large values of S were measured near the ground, but this time in deeper radiation fog.

Those large measured values of S were unexpected, given the predictions of Roach (1976) and Brown (1980) that values of S in radiation fog were only several hundredths of 1%. Also, model results of Bott et al. (1990) showed slightly subsaturated conditions near the ground in several types of radiation fog. The measured values of S were more like those predicted to exist in the updrafts of clouds (e.g., Warner 1968; Bower and Choularton 1988). Surprising results were also obtained with a droplet spectrometer during the 1982 Fog Project. Larger-than-expected droplets, often near the 40-μm droplet-diameter coalescence limit, formed rapidly in the radiation fogs. Similar observations were made earlier by Pinnick et al. (1978) and Choularton et al. (1981); the latter argued that large supersaturation fluctuations near fog top due to entrainment of warm moist air, or the recyling to fog top of droplets to be exposed to the maximum radiative cooling, were possible mechanisms for generating the large droplets.

A possible interpretation of the measured values of S is to consider them in error, even though the design criteria of the saturation hygrometer called for a measurement range of S between -5% and $+5\%$ [relative humidity (RH) between 95% and 105%], and an accuracy near $S = 0$ of $S = 0.01\%$ (Gerber 1980). A claim that such criteria are met must be carefully substantiated, because of the extraordinary accuracy demanded for such measurements. Twomey (1986) writes that the measurement of S fluctuations demands that ". . . for water vapor density, errors could not exceed a few hundredths of a percent, while tempera-

* Present affiliation: Gerber Scientific, Inc.

Corresponding author address: Dr. Herman Gerber, 1643 Bentana Way, Reston, VA 22090.

ture errors would have to be less than a hundredth of a degree." It is not possible to substantiate the performance of the saturation hygrometer by comparing it against either of the other means of measuring atmospheric RH, which are much less accurate, or the NBS standard humidity generator, whose upper limit is 98% ± 0.2% RH (Hasegawa and Little 1977). Judgment on the claimed accuracy of the hygrometer must rely on a demonstration that the instrument is based on firm physical grounds. Section 2 reviews the principle of operation of this hygrometer and its performance during the 1982 Fog Project. Appendix A details the means for calibrating the hygrometer.

The topic of droplet growth by condensation or evaporation in warm clouds and fog has evoked a large amount of discussion in the recent literature; a partial list includes Rodhe (1962), Baker and Latham (1979), Manton (1979), Clark and Hall (1979), Telford and Chai (1980), Telford and Wagner (1981), Jonas and Mason (1982), Baker et al. (1984), Paluch and Knight (1986), Paluch and Baumgardner (1989), Cooper (1989), Jensen and Baker (1989), and Bott et al. (1990). These papers have in common that they attempt to explain observed droplet spectra by specifying a relationship among turbulence, the moisture and temperature field, and the particle and droplet content. A frequent goal is to explain the source of large droplets required to initiate precipitation in warm clouds; this goal has proved to be elusive. The approach of the present paper is the same as the preceding, with turbulence playing a central role in the explanation of the measured supersaturation transients and the droplet spectral evolution in the radiation fog. However, the present work differs in one important respect: most of the preceding work deals with clouds in which rising air produces supersaturations that force the droplet spectrum. In the present case, supersaturations do not appear to be a result of this mechanism, because the measurements were made 1.0 m above a grassy surface for the Lake Fairfax case and 1.5 m over a similar surface during the ASRC experiment. At these low levels, vertical motions are largely damped out. Advection over horizontal temperature gradients also did not appear to be the cause of fog formation and supersaturation transients, because advection was weak and occurred over a broad flat grassy area. Thus, the cause of the supersaturations must be sought elsewhere. Broadwell and Breidenthal's (1982) ideas on nongradient turbulent diffusion and the application of those ideas to the interaction of turbulence with cloud droplets by Baker et al. (1984) and Jensen and Baker (1989) are evaluated as a possible mechanism for explaining the present observations.

In the following sections, experimental aspects are given first. Instrumentation is described, including instruments operated by ASRC during the 1982 Fog Project; and measurements are presented of radiation fog occurring on the morning of 6 October and 27 October 1982 at Albany County Airport, New York.

The second section gives the interpretation of the measurements in two parts. In the first part, the time-dependent mass balance equation for total water substance is derived for the case of turbulent mixing of two saturated parcels of air at constant pressure according to the Broadwell–Breidenthal (1982) mechanism. The predicted supersaturations are compared to the supersaturation measurements in the 6 October and 27 October fogs. In the second part, a simple model of inhomogeneous isotropic turbulence, based on conclusions reached in the first part, is used to mix parcels of different size and relative humidity. The model mixes parcels using the Monte Carlo approach, for which parcel size and moisture probability distributions are estimated from the saturation hygrometer measurements. The model includes quasi-Lagrangian droplet size calculations, which are compared to the measured droplet size distributions in the radiation fog. Due to the intractable nature of the droplet growth equation, such stochastic droplet growth calculations are usually considered impractical, because of large requirements for computer time. Appendix B offers a new set of time-dependent analytical expressions for calculating the change in droplet size due to condensational growth, under the condition that RH is specified. Those equations, used in the mixing model, permit efficient calculations over a wide range of droplet sizes, and give the proper transitions between growing, evaporating, and unactivated droplets and condensation nuclei.

The final section presents our conclusions. We speculate on the application of the results to clouds, and some suggestions are made for advancing the field given the current approach.

2. Instrumentation

The idea for the saturation hygrometer is based on observations made by Wylie et al. (1965) on the behavior of water droplets on the light-reflecting substrate of a dewpoint hygrometer. They found that when the substrate was treated with a hydrophobic film, it was possible to grow and evaporate the droplets with hardly any change in their number, even when the substrate was exposed to a room filled with aerosol. They further suggested that changes in the light-scattering power of the droplets on the hydrophobic substrate would indicate growth or evaporation of the droplets, and would permit equilibrium conditions to be determined. Without this hydrophobic film the number of droplets changes unpredictably (Davies 1963), and causes the accuracy limit of about 2% RH for dewpoint hygrometers (Wylie et al. 1965).

The saturation hygrometer uses a mirror coated with a hydrophobic film on which salt condensation nuclei are deposited and form centers of water condensation.

The growth of the droplets formed on the nuclei at high humidities is monitored optically (Fig. 1). To test the observations of Wylie et al. (1965), the hygrometer was placed in a metal box with inside walls wetted with distilled water and outside walls heavily insulated thermally. After several hours the light scatted by the droplets reached a plateau, which was highly reproducible, even after most measurements with the hygrometer in the radiation fogs. It was assumed that RH in this wet box reached 100.00%.

From the Köhler curves (e.g., see Twomey 1977) we see that the size of salt solution droplets is highly sensitive to RH near 100%. For example, 2.5-μm radius droplets at equilibrium at $S = 0$ reduce their radius by about 20% when $S = -0.2\%$. Given that the light scattered by the droplets depends on their radius squared, sufficient sensitivity may be available to sense even smaller changes in S with the saturation hygrometer, and thus meet Twomey's (1986) accuracy requirement for measuring supersaturation fluctuations. The size of the droplets on the hygrometer's mirror, as well as the mirror's dimensions and composition, affect the time response of the hygrometer, as shown by Gerber (1980). The dimensions of the hygrometer mirror used during the 1982 Fog Project were 1 cm $\times$ 1 cm $\times$ 1.27 $\times 10^{-2}$ cm, and the size of the salt solution droplets at equilibrium at RH = 100.00% was about 5-μm diameter.

The Köhler curves also show that when S in the atmosphere exceeds a critical value S_c, found for the droplets at S just greater than 0, the droplets grow without limit. Under those conditions the droplets on the hygrometer's mirror could grow sufficiently to coalesce into larger droplets, which would destroy the reversibility of the relationship between the hygrometer's optical signal and droplet growth. To prevent this from happening, infrared heaters warm the mirror whenever the ambient value of S is supersaturated (RH exceeds 100%) (see Fig. 1). The temperature increase of the mirror is related to the ambient value of S, as in the saturated salt hygrometer of Nelson and Amdur (1965).

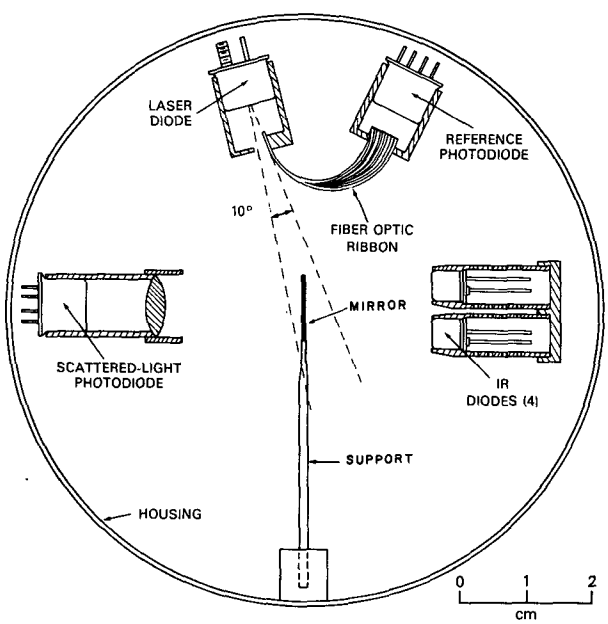

FIG. 1. Head-on view to scale of the saturation hygrometer sensor head.

The saturation hygrometer produces two channels of output. One channel functions when RH < 100%, and the other when RH > 100%. The switch between channels is fixed by determining the hygrometer's response in the wet box. The means for calibrating the hygrometer for RH larger and smaller than 100.00% is detailed in appendix A.

For proper operation it is essential that the hygrometer's mirror as well as the salt solution droplets on it closely track the ambient temperature. The heat exchange between the mirror and the ambient air must be rapid, while several potentially disruptive sources of heat must be accounted for. To maximize the heat exchange with the ambient air a thermally thin mirror of small thermal mass and large surface-to-volume ratio is used, and air is aspirated past the mirror to enhance surface heat conduction. Heat conduction to the mirror through the supporting stem must be minimized; this is done by choosing a stem with low heat conductivity, and with a small cross section. It has been shown (Brown 1980; Davies 1985) that droplets interact significantly with the ambient radiation field. This also applies to the droplets on the mirror, as well as to the mirror itself. To minimize blackbody cooling or heating of the mirror and droplets, a mirror with high broadband reflectivity (0.92) is used. With a desired error limit in the measurement of S of 0.01%, the maximum permissible difference between the temperature of the mirror and the environmental blackbody temperature is estimated from Newton's and Stefan's laws to be 1.8°C. It is unlikely that this temperature difference is exceeded, because the mirror is placed within a thermally thin radiation shield consisting of 0.00254-cm–thick metallized Mylar film coated with broadband light-absorbing paint on the inside surface.

The performance of the hygrometer, estimated from 25 hours of operation during the Fog Project, is summarized as follows:

1) The accuracy of the hygrometer was estimated to be approximately $S = 0.02\%$ near 100% RH, 0.1% at 99% RH, 0.3% at 98% RH, and 0.6% at 97% RH. Those values are based on wet-box calibrations, the reproducibility of those calibrations, and the assumption that RH = 100.00% in the wet box.

2) The optical characteristics of the droplet deposit

on the hygrometer mirror remained constant under conditions including moderate fog.

3) The droplet deposit changed during a dense fog when the ambient droplet guard (see Gerber 1980) overloaded.

4) The $1/e$ time response of the hygrometer to simulated step changes in RH was found to be 2.25 s.

5) No hysteresis was detected in the hygrometer output for negative and positive changes in RH.

Temperature was measured in the immediate vicinity of the hygrometer during both fogs with a thermistor (Yellow Springs Inc., YSI 44202) with a time constant of about 5 s. Wind speed was measured in the same location during the 27 October fog with a Thermal Systems Inc. omnidirectional hot sphere probe (Model 1620-12) with an accuracy of 1 cm s^{-1}.

The ASRC field site included a large number of other instruments, as detailed by Meyer et al. (1986). The ASRC instruments for which measurements are presented or discussed here include the following. Gill propeller anemometers were located at the 1-m level and three higher levels on a 16-m tower located about 40 m from the saturation hygrometer. Wet- and dry-bulb temperatures were measured at nine levels on the tower. An AEG visibility meter and a Particle Measuring Systems FSSP-100 were located near the tower and 1.5 m above the grass. The FSSP-100 produced 32 channels of particle size data, ranging from 0.5 to 47 μm in diameter.

3. Measurements

A 5-h record of saturation hygrometer, wind speed, and temperature measurements at the 1.5-m height above the grass at Albany County Airport prior to and during the fog episodes on 6 October and 27 October is shown in Fig. 2. The RH data is given as 1-min running mean values. In both cases the temperature gradually decreased under clear sky conditions, and fog formed 35 min after sunrise. The chosen criterion for fog formation, a reading of the AEG visibility meter of less than 1 km (see dashed lines in Fig. 2), coincided closely with the appearance of activated fog droplets. The wind speed was generally much less than 1 m s^{-1}; wind data is missing for the 6 October fog, because of the ~20 cm s^{-1} threshold wind speed of the Gill anemometer.

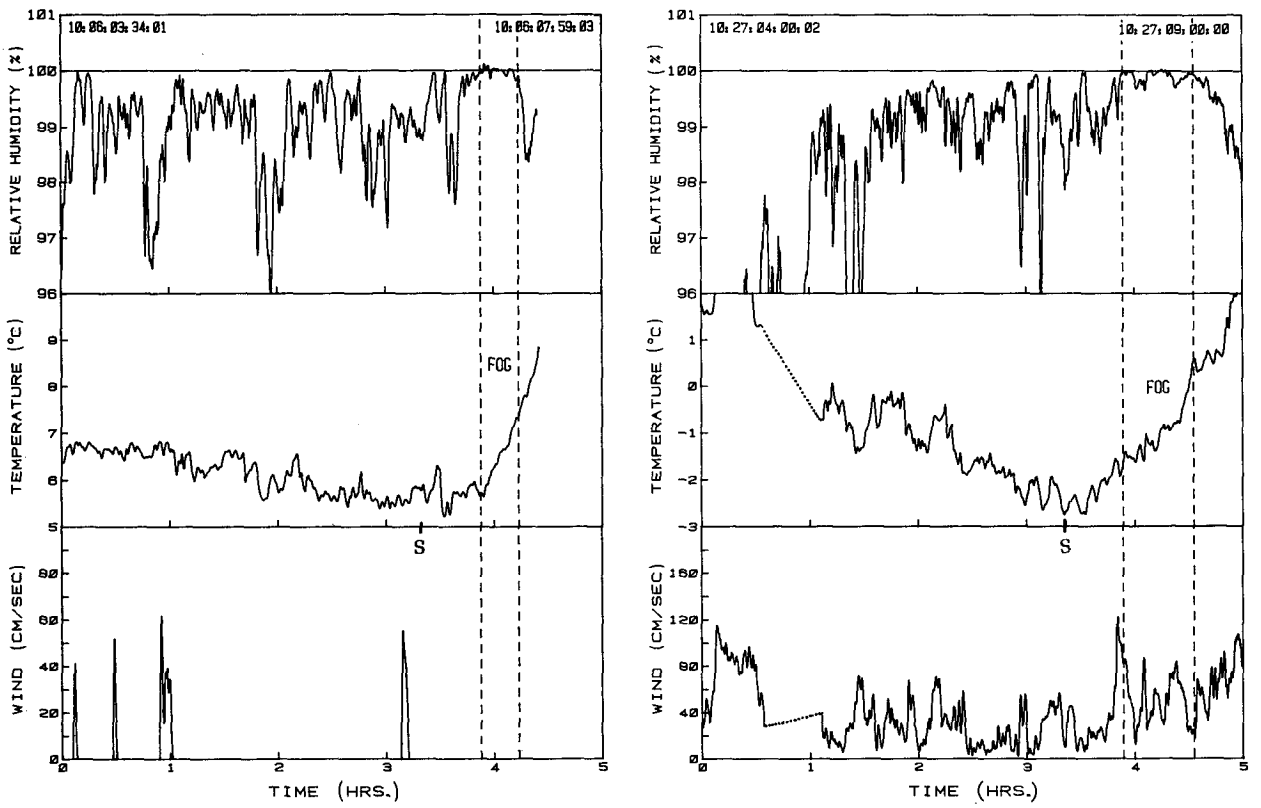

FIG. 2. Measurements of relative humidity, temperature, and wind speed 1.5 m above the grass surface at Albany County Airport for a 5-h period on 6 and 27 Oct 1982. Data consist of 1-min running means. Dashed lines bracket the period of fog observed near the surface; *S* denotes sunrise; and numbers in the upper corners refer to the beginning and end of the 5-h period by month:day:h:min:s.

Details of the temperature records suggest different formation mechanisms for the two fogs. The temperature at 1.5 m remained steady for 35 min after sunrise for the 6 October case, and then increased at the rapid rate of 6°C h^{-1} at the time when fog formed. The temperature profiles measured from the tower showed that the 16-m layer adjacent to the ground consisted of nearly saturated air with a stable lapse rate of −3°C/16 m when the fog first formed. The stability continued, but gradually decreased until 20 min later, when a warming surface caused an unstable lapse rate, and rapid mixing and fog dissipation. Those trends reflect a fog that was first observed to form aloft, and that shielded the near-surface layer from typical clear-sky radiative effects. It is proposed that the fog gradually lowered toward the ground due to turbulent mixing of warm saturated air with the cooler saturated layer near the surface, as in the mechanism discussed by Rodhe (1962). The gradual erosion of this stable layer was not caused by heating of the ground as shown by the stable lapse rate, but was likely due to mixing caused by shear and or buoyancy production higher in the fog.

The 27 October episode showed the expected steady increase in temperature after sunrise given clear sky conditions. This fog may have formed due to upward water vapor flux resulting from the sudden melting of frost on the grass, which coincided with the appearance of the fog.

Figures 3 and 4 show in greater detail the supersaturation hygrometer measurements during the two fogs. The values of S larger than saturation in the 6 October fog were obtained with the low-pass filter of the hygrometer in place; this reduced the time response of the instrument by a factor of about 10. All other data in these figures are given in unfiltered form with a time resolution equal to the 3-s digitizing rate of the data logger. In both fog cases the onset of the fog, as determined with the visibility meter, closely matched the time when the hygrometer first saw values in excess of RH = 100%. This independently supports the use of the wet box to set the hygrometer's 100% RH value, and suggests that measured values of RH on either side of RH = 100% are meaningful. The RH record in both fogs shows much fine structure, with transients in RH as large as 100% ± 0.4%. The record for the 27 October fog shows, in addition, two 5-min subsaturated periods in the fog when RH was as small as 99.5%. During these periods the fog has apparently advected from elsewhere and was in the process of evaporating.

The frequency distribution of RH during the two fogs is shown in Fig. 5; the two long subsaturated periods during the 27 October fog were arbitrarily not

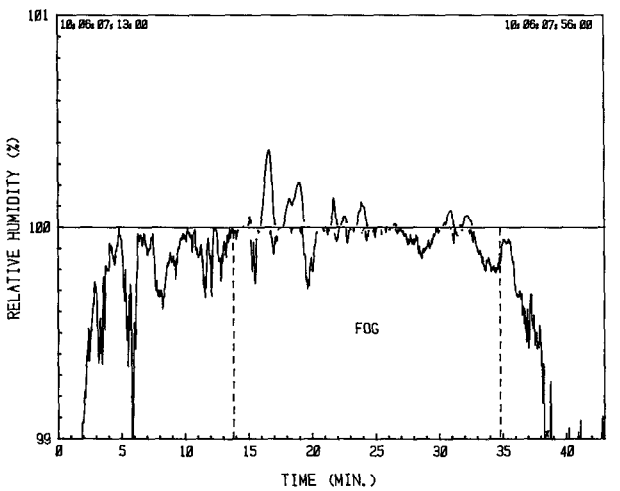

FIG. 3. High-resolution time record of relative humidity measured with the saturation hygrometer on 6 Oct. Dashed lines bracket the observed fog as in Fig. 2.

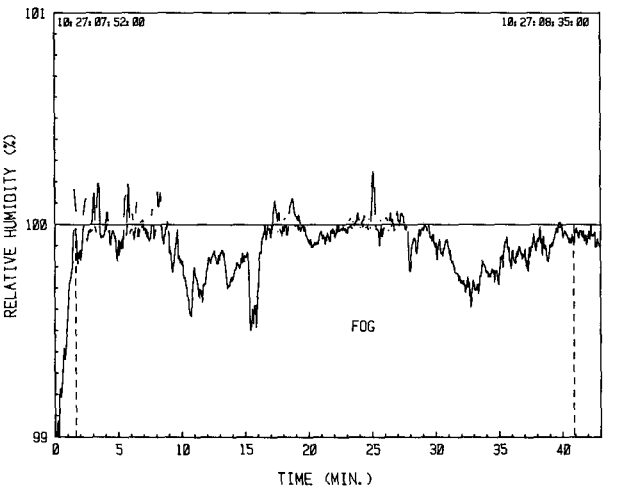

FIG. 4. Same as for Fig. 3, except for the 27 Oct fog.

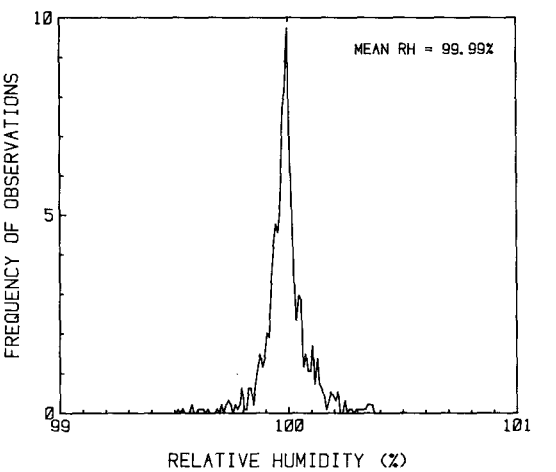

FIG. 5. Frequency distribution of relative humidity in fog constructed from data in Fig. 3 and Fig. 4 (see text).

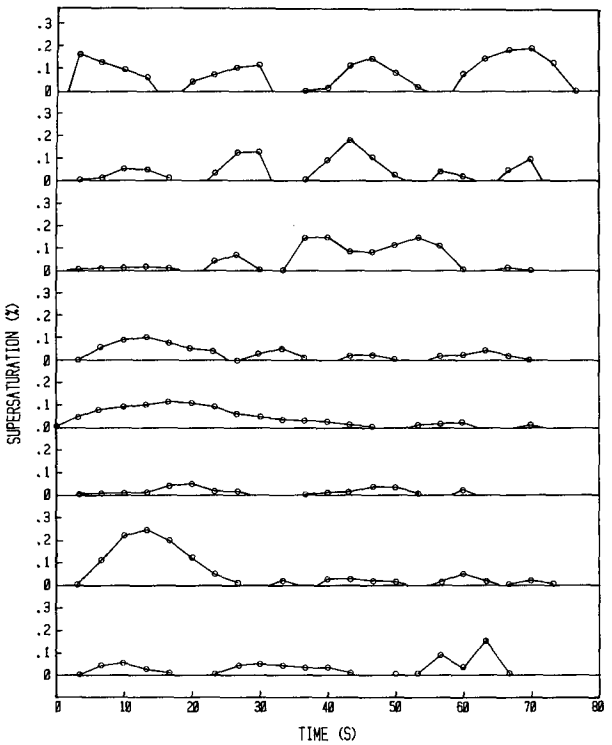

FIG. 6. Individual data points of relative humidity measured with the saturation hygrometer during periods of supersaturation in the 27 Oct fog.

included in this figure. As shown, the mean RH in the fogs is slightly less than 100.00%, with a symmetrical dropoff in the frequency on either side of the mean RH.

Figure 6 shows in even greater detail RH during periods of time when eddies in the 27 October fog showed RH > 100%. Given the Eulerian nature of the measurements, the curves in Fig. 6 do not directly indicate the lifetime of the supersaturated eddies, but only the time for the eddies to drift past the hygrometer. However, under the assumption that the average lifetime of the eddies reflected in the data in Fig. 6 does not change, the time intervals in Fig. 6 are indicative of typical eddy lifetimes. Figure 6 shows that this time can be on the order of tens of seconds, suggesting that the 2.25-s time response of the hygrometer is fast enough to provide useful information on the structure of these eddies. The visually observed drift of the fog droplets was nearly horizontal at all times, indicating that horizontal motions significantly exceeded vertical motions at the 1.5-m level in the fog.

Under the assumption that the supersaturated eddies do not change their characteristic lengths on the average during the time intervals shown in Fig. 6, it is possible to estimate those lengths by combining the data in Fig. 6 with the wind speed measured with the hot sphere. The lengths of the 32 supersaturated eddies of the 27 October fog are distributed about normally (sample standard deviation $s = 2.16$), their amplitude lognormally ($s = 3.06$), and their average shape is nearly a cosine curve, as shown in Fig. 7. The relatively slow response of the hygrometer strongly biases the statistics on eddy size, if much smaller supersaturated eddies exist, as is likely.

Size distributions of haze and fog droplets measured at the 1.5-m height just before and during the 6 October fog are shown in Fig. 8. The haze distribution labeled with the local time of 0715 was obtained several minutes before the onset of the fog when the saturation hygrometer showed RH ~ 100%. The other two distributions were each obtained 4 min later; they both show multiple peaks in the distributions, which are typical and even more evident in other radiation fogs (Jiusto and Lala 1983).

In the following analysis of the preceding data, the 6 October fog case will be looked at closely and conclusions drawn, with the assumption that eddy statistics from the 27 October fog also applied to the 6 October case. This is not a desirable approach, but must suffice because of the incomplete nature of this dataset and the greater complexity of the 27 October fog.

4. Interpretation

a. Nongradient mixing

As pointed out by Corrsin (1974), the use of the popular gradient diffusion models to determine tur-

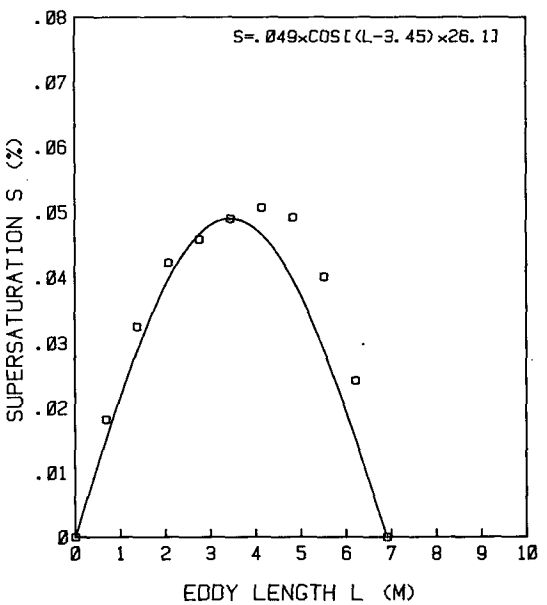

FIG. 7. Average shape of supersaturated eddies in the 27 Oct fog determined from Fig. 6 and wind speed measurements, normalized to the median eddy length of 6.9 m, and median peak supersaturation of 0.049%.

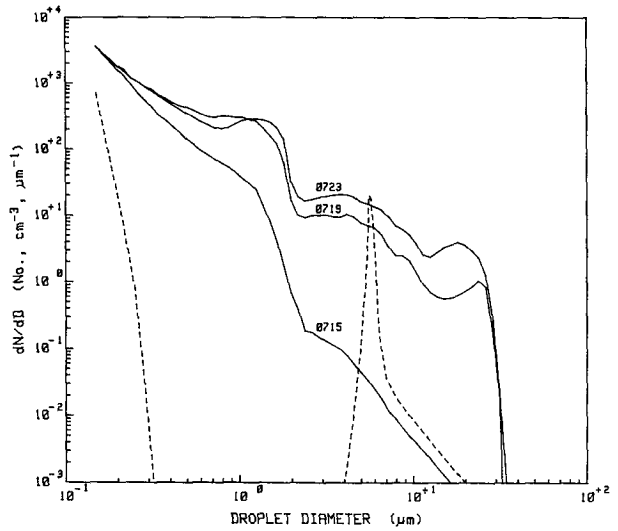

FIG. 8. Size distribution dN/dD of droplet diameters D measured 1.5 m above the surface at indicated local times on 6 Oct. Dashed curve results from classical condensational growth calculation with $S = 0.001$ for 5 min with 0715 as the initial distribution. Portion of dN/dD curves for $D < 0.5$ μm is extrapolated.

bulent transport is reasonably successful only when the scale of the turbulence is small in comparison to the distance across which the diffusing quantity is changing significantly. That the scale of the eddies in the fog appeared to be of the same order of magnitude as the height of the tower over which strong temperature gradients existed suggests that conditions for gradient diffusion of temperature and water vapor were not met in the 6 October fog. Baker et al. (1984) also suggested that gradient diffusion does not hold for atmospheric processes, such as the phase change of water vapor to liquid, that are nonlinear in the concentrations of the fluids being mixed. We apply instead the concept of nongradient mixing described by Broadwell and Breidenthal (1982) and Broadwell and Mungal (1988) in an attempt to explain the mixing in the 6 October fog. They showed experimentally that mixing of two species in turbulent shear layers was not gradient mixing, but consisted in essence of a two-stage process where the identity of the species remained largely intact while being mixed throughout the turbulent layer by larger-scale inviscid motions, and where homogenization of the species occurred only by molecular diffusion near the interface created between the species during the mixing process. The rate of homogenization was minimal until the turbulence scale approached the Kolmogorov microscale when the interface rapidly increased. They formulated a simple model based on their observations; Baker et al. (1984) discussed the implications of this model for mixing in clouds, and Jensen and Baker (1989) applied the model to calculate the droplet spectral evolution in an eddy consisting of cloudy air mixing with entrained subsaturated air.

The nongradient mixing model is applied to one eddy of the 6 October fog for the purpose of developing an expression for the time evolution of supersaturation S, which is then compared to S measured in the fog. Assumptions are made that mixing in this fog is caused by shear and that the eddy is composed initially of two unmixed parcels of equal volume and saturated air at two different temperatures, T_1 and T_2. Supersaturated vapor is released at the interface created between the mixing parcels in the eddy, because of the nonlinear dependence of the saturation vapor pressure on temperature. Further assumptions are made that the time constant for supersaturation released by molecular diffusion near each small area of the interface is negligible in comparison to the time constant of the vapor–liquid phase change, and to the time constant for the complete homogenization of the eddy. These assumptions appear reasonable given that the molecular diffusion rapidly becomes ineffective as the turbulence scale in the eddy increases much beyond the Kolmogorov microscale, and that the dissipation time constant of the microscale is at least an order of magnitude smaller than the time constants of droplet response and complete homogenization for typical initial eddy scales and turbulence levels (see Jensen and Baker 1989).

The classical expression for S (e.g., see Howell 1949; Squires 1952),

$$\frac{dS}{dt} = Q_1 \frac{dh}{dt} - Q_2 \frac{dw}{dt} \tag{1}$$

describes the balance of the rate of change of total water mass in a cloud updraft and has formed the basis for many cloud microphysical calculations made over the past 40 years. A modified version of Eq. (1) is applied to the present fog case. The vapor source term [first term on right side of Eq. (1)] is rederived, because the release of supersaturated vapor in the fog is related to molecular processes at the interface of the mixing saturated parcels in the eddy and the change in height h of the eddy is assumed negligible. The sink term (second term on right) describes the phase change of supersaturated vapor to liquid of the droplets and remains essentially unchanged from before, except that the thermodynamic coefficient Q_2 is reevaluated; w is the liquid water mixing ratio.

The rate at which supersaturated vapor is released by nongradient mixing is written as proportional to the rate of interface created in the eddy as it decays, so that the source term of Eq. (1) becomes

$$\frac{d}{dt}\left(\frac{x}{x_m} - 1\right) = C_1 \frac{dI}{dt}, \tag{2}$$

where x is the eddy vapor mixing ratio, x_m is the eddy saturation vapor mixing ratio after molecular diffusion has eliminated temperature and vapor gradients at the interface, C_1 is a constant, and I is the surface area of

interface per unit mass of the eddy. The expression (Baker et al. 1984)

$$I \approx \frac{1}{L}\left(1 - \frac{t}{\tau_L}\right)^{-3/2} \tag{3}$$

follows directly from Broadwell and Breidenthal's model; L is considered to be the scale of the shear layer, as well as the length scale of the eddy, and

$$\tau_L = \left(\frac{L^2}{\epsilon}\right)^{1/3} \tag{4}$$

is the time for complete homogenization of the eddy, where ϵ is the turbulent kinetic energy dissipation rate.

The treatment by Broadwell and Breidenthal (1982) includes the assumptions that mixing and dissipation in the eddy apply only to the inertial subrange of turbulence with a constant kinetic energy flux from larger to smaller scales and that the decay time of each scale is proportional to its linear dimension λ and characteristic velocity. This leads to a physical picture of mixing where all portions of the eddy change to smaller scales simultaneously so that at any given time the turbulence is homogenous.

The expression for C_1 in Eq. (2) is established by noting that for any time interval, $t_b - t_a$, the fraction of the maximum supersaturation $S_{\max}$ released by the decay of the eddy is given by the fraction of the total interface $I_{\max}$ created in the eddy during the same time interval:

$$\int_{t_a}^{t_b} \frac{1}{x_m}\frac{dx}{dt}\,dt \Big/ S_{\max} = \int_{t_a}^{t_b} \frac{dI}{dt}\,dt \Big/ I_{\max}, \tag{5}$$

which combined with Eq. (2) gives

$$C_1 = \frac{S_{\max}}{I_{\max}}, \tag{6}$$

where

$$S_{\max} = \frac{x_0 - x_m}{x_m} \tag{7}$$

and x_0 is the mixing ratio after homogenization of the equal volume parcels originally at T_1 and T_2 and at $\bar{T} = (T_1 + T_2)/2$ after mixing. The value of x_m corresponds to the temperature $T = \bar{T} + \Delta T$, where ΔT results from heating of the air by the release of latent heat of condensation L_h from the phase change. Here x_m is written in terms of T_1, T_2, x_s, and Δw by applying the small temperature-change approximation of the Clausius–Clapeyron equation and the First Law of Thermodynamics under isobaric conditions; x_s is the saturation mixing ratio at $\bar{T}$, and Δw is the amount of new liquid formed by the mixing.

By evaluating Eq. (3) for the time t_k required for the eddy to reach the Kolmogorov microscale, $I_{\max}$ is estimated

$$I_{\max} \approx \frac{1}{L}\left(1 - \frac{t_k}{\tau_L}\right)^{-3/2}, \tag{8}$$

where the expressions for

$$t_k \approx \tau_L\left[1 - \left(\frac{\lambda_k}{L}\right)^{2/3}\right] \tag{9}$$

and the scale length of the microscale

$$\lambda_k = \left(\frac{\nu^3}{\epsilon}\right)^{1/4} \tag{10}$$

come from Broadwell and Breidenthal's model; ν is the kinematic viscosity.

The sink term of Eq. (1) describes the loss of supersaturated vapor to the growing droplets in the eddy. According to Fletcher (1966),

$$\frac{dw}{dt} = \int_r 4\pi\rho r^2 \frac{dr}{dt}\frac{dN}{dr}\,dr \tag{11}$$

where r is the droplet radius, ρ is the droplet density, and dN/dr is the droplet size distribution (number of droplets per unit droplet dimension per unit eddy volume).

For the present case

$$Q_2 = \frac{1}{\rho_s x_s K} \tag{12}$$

$$K = \frac{L_h^2 M_w \Delta w}{R\bar{T}^2 c_p} + 1 \tag{13}$$

where ρ_s is the air density at $\bar{T}$, M_w is the molecular weight of water, and c_p is the specific heat capacity of water.

The droplet growth equation used with Eq. (11) is given by (Pruppacher and Klett 1978)

$$r\frac{dr}{dt} = C\left(S - \frac{A}{r} + \frac{Br_d^3}{r^3}\right) \tag{14}$$

where C contains the accommodation α_T and condensation α_c coefficients, A and B are slowly varying functions of primarily temperature and the salt content of the droplets, and r_d is the dry radius of the condensation nucleus.

The use of Eqs. (11) and (14) in the present context requires the assumption that all droplets per unit mass (or unit volume) of the eddy compete equally for the supersaturated vapor released in the fraction of the unit eddy volume consisting of the interface area times a finite interface thickness. This assumption gives reasonable results, because Eqs. (11) and (14) show that dw/dt is approximately proportional to the supersat-

uration times the number of droplets affected. Thus, the fraction of droplets in the interface volume exposed to the interface supersaturation should have about the same effect on dw/dt as all the droplets per unit eddy volume exposed to the interface supersaturation averaged over the unit volume. The assumption causes least error when small changes occur in dw/dt, and causes an underestimate in dw/dt when large changes occur in r.

Combining Eqs. (2)–(10) gives the source term of Eq. (1), and combining Eqs. (11)–(14) gives the sink term of Eq. (1), which are integrated over time with the initial condition of $S = 0$ for $t = 0s$ to yield the desired result:

$$S \approx \left(\frac{x_0}{x_s K} - 1\right)\left(1 - \frac{t_k}{\tau_L}\right)^{3/2}\left(1 - \frac{t}{\tau_L}\right)^{-3/2} - \frac{1}{\rho_s x_s K}\int_t\int_r 4\pi r \rho C\left(S - \frac{A}{r} + \frac{Br_d^3}{r^3}\right)\frac{dN}{dr}\,dr dt. \quad (15)$$

Equation (15) is numerically evaluated under the following conditions: dN/dr is given by the size distributions measured at 0715 or 0719 local time on 6 October (Fig. 8), or by the distribution at 0719 multiplied by a factor of 10; $T_1 = 278$ K and $T_2 = 281$ K correspond to temperatures measured near the surface and on the top of the 16-m tower at 0715; $L = 6.9$ m is the median eddy length scale (Fig. 7); $A = 1.13 \times 10^{-7}$ cm, $B = 0.60$, and $C = 7.98 \times 10^{-7}$ cm^2 s^{-1} at $\bar{T} = 279.5$ K and for $(NH_4)_2SO_4$ nuclei; $\alpha_T = 1.00$; $\alpha_c = 0.04$; $S_{max} = 0.433\%$; $t_k = 36.121$ s for an assumed value of $\epsilon = 10$ cm^2 s^{-3}; and $\tau_L = 36.244$ s.

Results of the calculations, given in Fig. 9, show that nongradient mixing of saturated air at different temperatures causes supersaturation transients, which supports the hypothesis that the transients of S in the 6 October fog were caused by such mixing. Figure 9 shows a steep increase of S at $t \sim t_k$, and a peak value of S close to $S_{max} = 0.433\%$. The rapid change in S occurs because the model predicts a rapid increase of the interface between the mixing parcels just before complete homogenization of the eddy, and because the response of the droplets to the supersaturated vapor is slower than its release.

As a consequence of the predicted rapid release of S, all droplets in the eddy are exposed to nearly uniform values of S, consistent with the "homogeneous" mixing concept (see Baker and Latham 1979). A similar conclusion was reached by Jensen and Baker (1989), who applied nongradient mixing to a 1D model, where molecular diffusion of heat and vapor was included in calculating the mixing of cloudy air with drier clean air at the same temperature.

The calculations using Eq. (15) were repeated with the parameter S in the sink term changed to S_{max}. The former parameter was expected to underestimate the loss of vapor to growing droplets when large changes in droplet size occurred, while the latter should overestimate the loss. Thus, the best estimate of vapor loss is somewhere in between. Curves of S versus t (not shown) with S_{max} used in Eq. (15) are approximately the same shape and have nearly the same maximum values of S as the curves in Fig. 9. This suggests that the exact physical description in the model of the moisture and temperature fields in the eddy is not crucial, whereas the expression for the rate of interface created in the eddy [Eq. (3)] has an overwhelming effect.

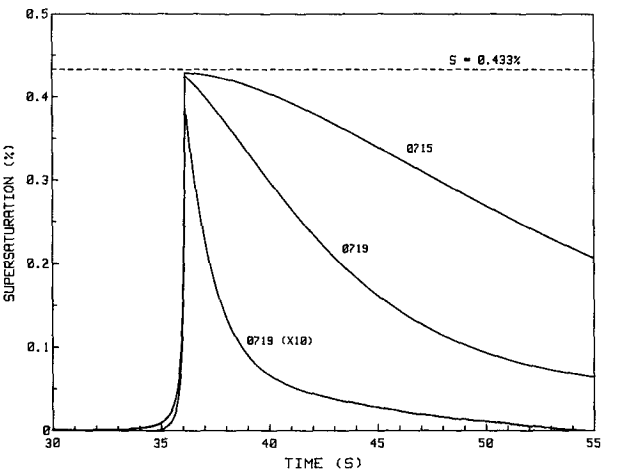

FIG. 9. Calculated time evolution of supersaturation S for mixing of two saturated parcels of equal volume and with a temperature difference of 3°C according to the Broadwell–Breidenthal (1982) nongradient mixing mechanism as described by Eq. (15). Solid curves give predicted S for different initial droplet size distributions given for the same local times as in Fig. 8. Dashed line is the maximum S possible from mixing parcels when no vapor-to-liquid conversion takes place.

The maximum values and durations of S in Fig. 9 agree favorably with S measured in the 6 October fog (Fig. 3); however, the shape of the calculated S transients are unlike the shape of those measured in Figs. 6 and 7. The measured transients are symmetrical on the average, and do not show the initial rapid increase and exponential decrease of S of the calculated transients. This difference suggests that assumptions of homogeneous turbulence, and the simultaneous decrease in the length scale in the eddy, as specified in this model, oversimplify the mixing process. Improvement in the model may require a much more sophisticated derivation of the rate at which interface is created in a dissipating eddy (e.g., see Pope 1988).

b. Stochastic droplet growth

In this section we estimate whether the observed transient supersaturations caused the rapid increase of droplet sizes and the broadening of the droplet spectra

measured in the 6 October fog. This is done with a simple stochastic mixing model that uses the Monte Carlo approach to randomly mix pairs of air parcels whose scale and supersaturation statistics are estimated from the hygrometer and hot-sphere wind measurements. In essence, this model applies the "favored-droplet hypothesis," where, due to the statistical nature of turbulence, some "favored" droplets experience a time history in the fog that is more conducive to condensational growth than other droplets, causing the finite probability of the appearance of some large droplets.

This approach was chosen because a less complicated droplet growth calculation, where a constant or "effective supersaturation" (Hudson 1980) is applied to the droplets in the 6 October fog, gives unrealistic results. For example, when $S = 0.1\%$ is applied to the initial 0715 spectrum of the fog for 5 min, a narrow peak separated from the smaller particles develops in the spectrum. This peak is unrealistic, but typical of droplet calculations where the effect of mixing is not considered (Pruppacher and Klett 1978). Continuous turbulent mixing in the 6 October fog is suggested by the fluctuations in the measured S, and by the changing vertical temperature profile.

The present model simulates continuous mixing throughout the fog as follows. The fog is divided into a first ($m = 1$) ensemble of k_0 different air parcels, each with its own value of length scale L and droplet spectrum. Next, k_0 random pairs of parcels from the ensemble are chosen, each pair is mixed in an eddy, S of the mixture is chosen at random, and the droplets in the mixture are permitted to react. The droplets in all eddies start growth at the same time. Growth proceeds for a time τ_m which is the unknown time between mixing events in the fog. After τ_m, the k_0 mixtures with their new droplet spectra are placed in a second ($m = 2$) ensemble for which mixing and droplet growth again takes place for k_0 random eddy pairs with new random choices made for L of the parcels and S of each mixture. Subsequent ensembles continue the mixing process and droplet spectral evolution in the same way.

In the Monte Carlo approach the choice of L and S requires the use of the cumulative (probability) distribution function (CDF) of each parameter. The structure of the "eddies" in Figs. 4 and 6 and wind speed are used to estimate the scale of the parcels in constructing the CDF of L. The data do not reveal what part of the observed RH structure corresponds to parcels or eddies, which are defined as mixtures of the parcels, in the model. We simply assume that the boundaries and scale L of individual parcels are defined by locations in the RH record where $S = 0$. The CDF for L established in this way from the 27 October fog data is shown in Fig. 10. The CDF for S is estimated

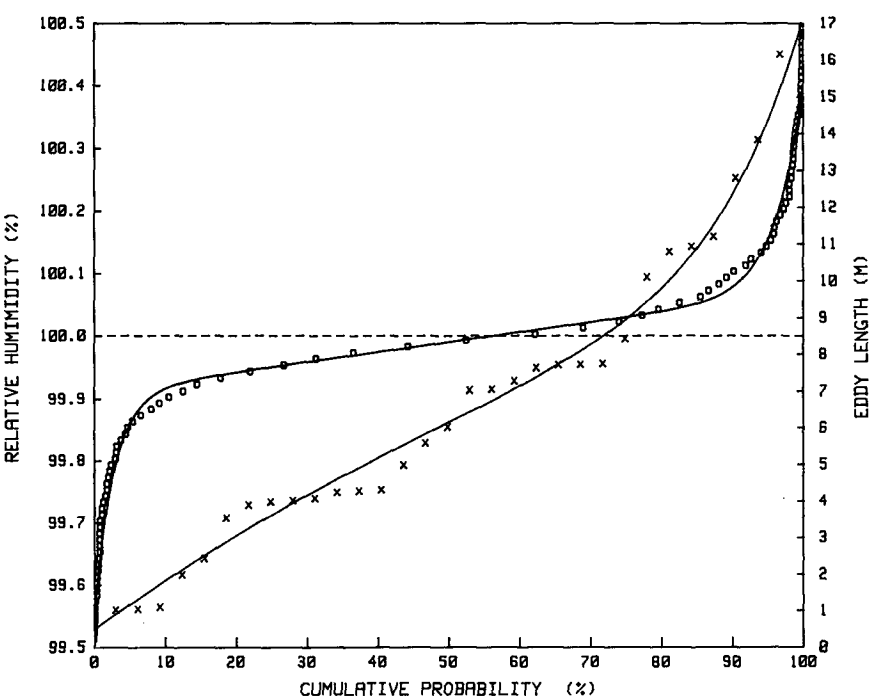

FIG. 10. Cumulative probability of relative humidity RH (circles, O) determined by integrating the frequency distribution of RH in Fig. 5; and the cumulative probability of eddy length (crosses, ×) determined by combining eddy duration given in Fig. 6 with wind speed measurements for the 27 Oct fog.

by integrating the frequency distribution of S, compiled from both 6 October and 27 October fogs, shown in Fig. 5. Figure 10 shows both CDF and fitted analytical expressions of the form

$$\text{RH}\,(\%);\ L\,(\text{m}) = [(A \times P) + B] \times [1 - \{\exp[-(C \times P) - D]\}^{1.2}] \times [1 + (E \times P^F)] \quad (16)$$

where $A = 9$, $B = 1.7$, $C = 7$, $D = 0.3$, $E = 0.6$, and $F = 8$ for the CDF of L; $A = 0.16$, $B = 99.91$, $C = 30$, $D = 4.7$, $E = 0.0033$, and $F = 25$ for the CDF of RH [or $(S + 1) \times 100\%$]; and P is the cumulative probability (0 to 1) of the parameter. The random choice of S and L is made by operating on each CDF with P chosen at random from a uniform distribution function. This process produces choices of S and L that are uncorrelated.

In the preceding section it was concluded from calculations that nongradient turbulent mixing causes a rapid adjustment of supersaturation to $S_{\max}$ due to molecular diffusion when the Kolmogorov microscale is approached. This adjustment depends largely on the moisture and temperature of the mixing parcels, and is nearly independent of droplet content. This behavior permits S in Eq. (14) to be parameterized in terms of $S_{\max}$, and in terms of a time constant, $\tau = 1/(a_2 I_r)$, which characterizes the exponential approach of S to water saturation ($S = 0$) as the droplets respond to the excess or lack of vapor (Cooper 1989); τ is inversely proportional to the integral droplet radius $I_r = \int rdN/drdr$. Figure 9 illustrates that τ ranges from about 2 to tens of seconds. The model approximates the exponential behavior of S by applying a constant value of $S_{\max}$ to each eddy for a period of time equal to τ. Also, the assumption is made that the CDF for $S_{\max}$ is equivalent to the measured CDF of S; I_r corresponds to the integral radius before droplets grow. The magnitude of τ indicates that after some tens of seconds, S transients in the fog will decay, unless continuous mixing occurs. This permits us to roughly estimate a value for τ_m, which is chosen to be 60 s.

Several additional assumptions are included in the model:

1) The turbulent mixing in the 6 October fog is steady. This may have been true for mechanical mixing; however, the observed gradual decay in the amplitude of the S transients seen in the aging fog suggests that vapor and temperature gradients were gradually being reduced. Thus, from the standpoint of droplet forcing, the turbulence did not appear to be steady, and this assumption would tend to overestimate the forcing.

2) Turbulent mixing in the fog is isotropic.

3) There is no droplet sedimentation or coalescence.

4) Radiative effects on the growth of the droplets are not included.

5) There is sufficient liquid water content in the fog so that transients of S with RH < 100% decay to water saturation.

6) The S gradients caused by molecular diffusion at the interface of the mixing parcels have a negligible effect on the shape of the droplet spectra. This assumption is reasonable on the basis of the calculations by Jensen and Baker (1989), which showed that changes in the width of the droplet spectra due to such gradients were insignificant when differences in moisture content of the original two unmixed parcels were as small as measured typically in the 6 October fog.

The model is initialized by assigning the droplet spectra measured at 0715 to all parcels in the $m = 1$ ensemble. The spectra is divided into 53 geometrically equal size intervals ranging from 0.075-μm to 10-μm droplet radius. The corresponding 54 different size classes r and the number concentration N of the droplets in each size class are specified. The model also requires 54 values of r_d, which are determined by solving Eq. (14), given the observation that $S \sim 0$ at 0715, and the assumptions that $dr/dt = 0$, and that CCN consist of $(NH_4)_2SO_4$ nuclei.

The application of random values of L and $S_{\max}$ to k_0 parcel pairs for $m = 1$ results in k_0 mixtures with different size distributions. When pairs of these mixtures are themselves mixed ($m = 2$), the number of droplet size classes doubles. To avoid the unwieldy number of calculations that this doubling would require, the number of size classes are reduced back to 54 after growth of the droplets in each mixture is complete. The reduction is done by first sorting the droplets in the mixture according to size after growth and then combining adjacent size classes to yield new classes for use with the next value of m. Each new radius class is found by taking a volume average of the total volume contributed by droplets of two adjacent classes. Each contribution depends on r^3 and N of the adjacent size classes. The contribution of each N is weighted by the eddy volume L^3 normalized by the total volume of the mixture. The new radius class is given by

$$r_{i,k,m+1} = \left\{\left[N_{i,k,m}\left(\frac{L_k^3}{L_k^3 + L_{k+1}^3}\right) r_{i,k,m}^3 + N_{i+1,k+1,m}\left(\frac{L_{k+1}^3}{L_k^3 + L_{k+1}^3}\right) r_{i+1,k+1,m}^3\right] N_{i,k,m+1}^{-1}\right\}^{1/3} \quad (17)$$

where the concentration of droplets in the new radius class is

$$N_{i,k,m+1} = N_{i,k,m}\left(\frac{L_k^3}{L_k^3 + L_{k+1}^3}\right) + N_{i+1,k+1,m}\left(\frac{L_{k+1}^3}{L_k^3 + L_{k+1}^3}\right), \quad (18)$$

and $r_{i,k,m}$ and $r_{i+1,k+1,m}$ are defined as the adjacent radii classes i and $i+1$, $N_{i,k,m}$ and $N_{i+1,k+1,m}$ are the corresponding droplet concentrations, and L_k and L_{k+1} are the length scales of parcels k and $k+1$. Equations (17) and (18) serve to conserve N and LWC between adjacent droplet size classes, and to include the effect of variable L in the mixing process. Nucleus volume is conserved with a similar equation.

Numerical calculations using Eq. (14) usually specify fixed droplet size bins Δr in which droplets are placed after growth. In the present case bins are not used, because they can lead to numerical broadening of the droplet spectra in cases where the width of the bins and the amount of droplet forcing are insufficient to accurately reflect droplet size changes. In the present model, growth of the droplets occurring in small increments rather than large jumps makes the bin method difficult to use. Here droplet sizes and concentrations are dealt with individually, and only after completion of the entire mixing process is the typical representation of the droplet spectra, $\Delta N/\Delta r$, reconstructed from final values of r and N.

The following applications of the model use a modest value of $k_0 = 10$ for the number of parcels in the ensembles. Nevertheless, given the desire to model the fog for a maximum mixing time of 1 h, the number of radius classes and this value of k_0 leads to the requirement of applying Eq. (14) about 10^5 times. Numerically such a problem is cpu intensive, even for a large computer. This is caused by the well-known mathematical "stiffness" of Eq. (14), which must be integrated for each droplet over small time steps to avoid numerical instability (Aranson and Brown 1971). The time step is 0.01 s for droplets on the order of $r = 1$ μm (Bower and Choularton 1988) and is even smaller when an accurate evolution of smaller droplets and haze particles is desired.

Rather than applying a large computer to the present problem an effort was made to modify Eq. (14) to reduce cpu time. This was done to take full advantage of the constant value of S_{max} specified in the model for each eddy, and because a desirable goal of formulating cloud microphysical phenomena is to present them in a simple enough form to permit their practical parameterization in dynamic models, which themselves usually require supercomputers. As detailed in appendix B, Eq. (14) is rewritten to give a set of analytical expressions

$$r \approx f(r_0, S, t, r_d) \quad \text{for} \quad \begin{cases} r_d > 10^{-6} \text{ cm} \\ r_0 > r_d \\ S > -1 \\ t > 0 \text{ s} \\ \text{nucleus type} \end{cases} \qquad (19)$$

that give one-equation solutions to the time dependence of r, given the initial droplet radius r_0, S, t, r_d, and nucleus type over a range of values shown following the left-hand brace. This approach greatly speeds up the calculations, and properly accounts for the responses and transitions of nuclei and droplets to the fluctuations of S both greater and smaller than RH = 100%. Hänel (1987) gives a related treatment of droplet growth.

The first run of the model uses the CDFs given in Fig. 10, the initial dN/dD for 0715 given in Fig. 8, and the total mixing time of 15 min, which corresponds to 15 mixing events. The calculated size distribution is shown in Fig. 11. It was constructed by averaging dN/dD for the k_0 parcels of the final ensemble, $m = 15$. This is justified, because in the 120-s averaging time used in measuring dN/dD with the FSSP, about k_0 parcels flowed past this sensor given the mean parcel scale and a reasonable guess of the mean flow rate.

The results of the first run show a broadening of the size distribution from its initial shape, but fail to show the large 30-μm droplets measured at 0719 and 0723. The peak that developed in the modeled dN/dD between 2 and 10 μm formed in spite of the slightly undersaturated mean conditions (RH = 99.99%). This demonstrates that the stochastic approach used by this model produces favorable growth conditions for some droplets, even though the fog is less than saturated on the average. In the evolution of the modeled dN/dD, the liquid water content attains near equilibrium conditions after about $m = 5$, and only the droplet spectrum slowly broadens thereafter.

In the second run of the model the CDF for RH in Fig. 10 was biased by +0.1%, and all other aspects were kept the same. This was done in an attempt to generate

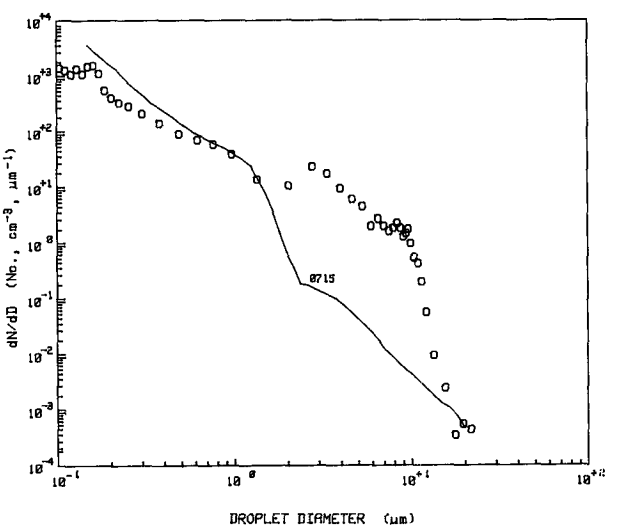

FIG. 11. Predicted evolution of dN/dD after 15 min according to the stochastic condensational growth model (see text) using the statistics in Fig. 10, and the 0715 distribution in Fig. 8 for initialization.

results corresponding to an upper limit for the nongradient mixing effect for the 6 October fog. This increase should more than compensate for saturation hygrometer errors, which were estimated to be one fifth as large, and to reduce the effects of subsaturated periods in the fog that may have advected past the sensors. The model results in Fig. 12 show the development of a narrower peak with droplets as large as 15 μm; however, the observed 30-μm droplets are again lacking.

From these results it is necessary to conclude that the nongradient mixing mechanism was not responsible for the appearance of the large droplets in the 6 October fog. This mechanism may have created the droplet-size peak between 2 and 15 μm in the fog; however, it appears that the inverse proportionality in the model between the relaxation time τ of the S transients and the integral radius I_r of the droplets tends to be a self-limiting effect, preventing droplets from growing much larger when I_r increases.

The final run shown in Fig. 13 shows the effect of uncoupling I_r from τ, which is given a constant value of 60 s; again $m = 15$ and a bias of RH = 0.1% were used. We find a better resemblance of the modeled dN/dD in Fig. 13 to the measured dN/dD, with some droplets predicted to be near 30 μm. The second peak in the predicted dN/dD resulted when a fraction of the size distributions in the final ensemble was averaged with a smaller fraction of size distributions from another ensemble for $m = 3$. This was done to see if droplets of different ages, and perhaps representing different formation mechanisms in the fog, would cause a double-peaked distribution as observed.

The results of the last run are speculative, because no measurements were made in the present study for identifying other droplet growth mechanisms. We speculate that the observed 30-μm droplets were formed higher up in the fog by much larger and perhaps lengthier periods of supersaturations caused by other factors, as discussed by Choularton et al. (1981), Davies (1985), Alves (1987), Davies and Alves (1989), and Bott et al. (1990); and that those droplets were mixed and sedimented downward to the 1.5-m level of the present observations. This has support from the observation that the 6 October fog formed 20 min earlier aloft. The application of the saturation hygrometer in a profiling mode in the fog, as well as measurements near fog top done in conjunction with radiation, temperature, and flux measurements are needed, if the source of such large droplets is to be identified.

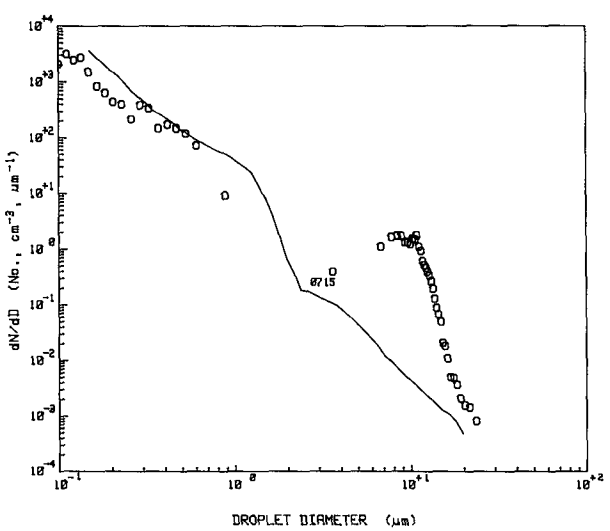

FIG. 12. Same as Fig. 11, except that supersaturation statistics in Fig. 10 are biased by RH = 0.1%.

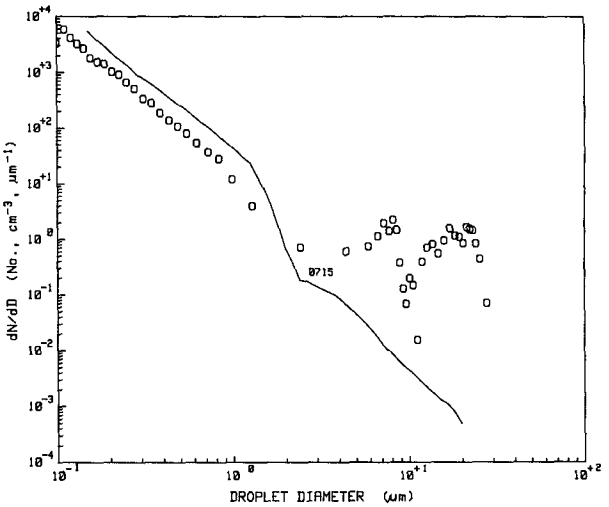

FIG. 13. Same as Fig. 12, except that a constant 60-s interval for droplet growth is used for each mixing event, instead of the inverse proportionality between the interval and the droplet integral radius (see text).

5. Discussion

We have shown that a possible explanation for the supersaturation transients observed in the 6 October and 27 October radiation fogs with the saturation hygrometer is the nongradient mixing of eddies, as discussed by Broadwell and Breidenthal (1982), Baker et al. (1984), and Jensen and Baker (1989). The supersaturation transients result because the release of excess vapor by molecular diffusion at the interfaces of nearly saturated air mixing in eddies is faster than the relaxation time of droplet response to this excess. This conclusion must be conditional, because of the subjective estimates of vertical wind speed made in these fogs. While this speed appeared negligible, any amount would have contributed to the measured RH. However, the very large supersaturations, perhaps approaching

1%, in the radiation fog observed at Lake Fairfax County Park support the present explanation, because this fog consisted of a shallow ground fog that had a nearly constant depth over the grassy surface and was exposed to a strong temperature gradient of about 8°C/2 m. Under those conditions nongradient mixing would cause the large observed supersaturations. Nevertheless, measurements with the saturation hygrometer in fog should be repeated to produce a more complete dataset including radiation and accurate vertical wind measurements.

Another concern for the explanation offered here for the supersaturation transients must be the difference between the shape of the calculated S transients (Fig 9) and the shape of the measured S transients (Fig. 6). The shapes were judged arbitrarily to be sufficiently similar to support the nongradient mixing concept. There is no explanation for this difference, except to say that the calculated transients depend perhaps on a turbulence dissipation model that is inadequate for the inertial subrange of turbulence.

As noted by Saxena and Fukuta (1982), the fluctuating S in the fogs makes it unrealistic to assign or deduce a constant value to S in fogs as done by Fitzgerald (1978), Hudson (1980), and Meyer et al. (1980). Their use of a constant value of S permits a one-to-one correspondence to be made between the cloud condensation nuclei (CCN) spectra and activation and growth of droplets. Clearly this is unrealistic, because the fluctuating value of S will activate CCN over a broad range in the activity spectrum. It is proposed that the nongradient mixing mechanism can be an effective means of activating new CCN entrained into fogs, as well as CCN already located in the interior of fogs. The effectiveness of this mixing depends on the value of the integral droplet radius and on the frequency and magnitude of temperature gradients in the near-saturated mixing environment.

Another consequence of nongradient mixing in fogs is that fog models that utilize K theory to parameterize turbulence (e.g., Rodhe 1962; Saxena and Fukuta 1982; Welch et al. 1986; Turton and Brown 1987; Bott et al. 1990) may not be capable of accurately describing microphysics such as droplet spectra when nongradient diffusion is important. Gradient mixing requires local turbulence closure where adjacent parcels exchange matter. This mixing would not cause the large S transients that drive droplet response in nongradient mixing, where the exchange of matter can occur for nonadjacent parcels with much larger differences. The present results suggest that an accurate description of microphysics may require the use of nonlocal turbulence closure such as, for example, in transilient turbulence theory as discussed by Stull (1984).

It also remains to be determined how important nongradient diffusion and its effect on microphysics are on the dynamic behavior of fog. While it may be true that a simple parameterization of microphysics in dynamic models would suffice in predicting the behavior of radiation fogs (Fitzjarrald and Lala 1989), this still needs to be demonstrated.

The accuracy of the model-predicted droplet spectral broadening in the 6 October fog is difficult to assess because of the unknown uncertainties in the assumptions used in formulating the stochastic mixing model and in constructing and applying the CDFs of supersaturation and eddy scale. Besides the uncertainties in constructing the CDFs mentioned earlier, another possible error source may be the assumption that the two CDFs are uncorrelated. According to nonlocal turbulence theory, large parcels contribute more strongly to mixing at greater distances from their origin than do small parcels. This suggests, in the present case for a saturated layer with a temperature gradient, that large parcels undergoing mixing will on the average cause greater supersaturation transients than small parcels, because the large parcels transport greater temperature differences. The neglect of this effect would cause the present model to underestimate droplet spectral broadening. Determination of the correlation between the CDFs requires a better dataset than collected here.

An obvious question to ask is: How do nongradient mixing and the present results for fog apply to clouds? Jensen and Baker (1989) partially answered this question when they considered the effects of mixing dry air into the side of a cloud. This mixing caused a shift of the droplet spectrum to smaller sizes with relatively small spectral broadening, unless the fraction of dry air introduced into the final mixture was large. Also, the resulting evaporation of droplets was closer to "homogeneous" than "inhomogeneous"; that is, the rapid final homogenization by molecular diffusion caused all droplets to see about the same RH, which is the same conclusion reached for the fog. The present study suggests that nongradient mixing may also be important within the cloud. This mixing may cause supersaturation transients that result in the activation of new CCN without the need for vertical motions, and it may cause significant spectral broadening when a succession of mixing events are considered. It is hypothesized that the spectral broadening is caused by the combination of different droplet spectra in mixing air parcels, while the nongradient aspect of this mixing results only in a shift of the combined spectrum in each eddy without much broadening, because of "homogeneous" mixing. Those effects are in addition to spectral changes caused by suggested interactions among vertical motions, entrainment, and turbulent mixing, which is the topic of many prior studies (Baker and Latham 1979; Manton 1979; Telford and Chai 1980; Cooper 1989; Hicks et al. 1990; and others). The present study is similar in its approach to the one used by Cooper (1989), who also used a statistical approach to look at spectral

changes of cloud droplets caused by fluctuations in the quasi-steady supersaturation S_{qs} due to mixing and turbulence-induced fluctuations in vertical velocity. The difference between these two studies is that the time constants associated with S transients in nongradient mixing are undoubtedly shorter than the time constants associated with fluctuations in S_{qs} due to vertical motions. That, in combination with the apparently self-limiting nature of droplet growth by nongradient mixing because of the inverse proportionality between the lifetime of the S transients and integral droplet radius, prevents nongradient mixing from producing, by itself, large droplets according to the "favored droplet hypothesis." This agrees with Cooper's (1989) assessment of nongradient mixing, which he judged less important for producing the large droplets in warm clouds than mixing correlated with updrafts and LWC. Nevertheless, the importance of nongradient mixing for clouds should be investigated because, under certain conditions, nongradient mixing may generate droplets without substantial updrafts, as in the fog, and play an important role in establishing microphysical and optical properties. Places to look for the effects of this mixing mechanism may be long-lived clouds with frequent mixing or near-saturated layers undergoing mixing. A candidate might be marine stratocumuli being mixed near their tops by entrainment induced by buoyancy or Kelvin–Helmholtz instability.

Only one saturation hygrometer, a laboratory version, was built 10 years ago. This instrument has proved its usefulness for measuring RH in fogs. However, it was only marginally successful in measuring RH from a tethered balloon in marine stratocumuli during the 1987 FIRE project off the West Coast (Albrecht et al. 1988; James et al. 1989). The lack of success was due to the high wind speeds encountered and the failure of the laboratory design to sufficiently dampen turbulence generated by the sensor. Given recent developments in laser diodes and ICs, it appears possible to build a practical and miniature atmospheric RH sensor based on the simple principles of the saturation hygrometer. This sensor could have a response time of 2 Hz and would be useful for surface, tower, free-flying or tethered balloon and perhaps also for slow-flying aircraft instrumentation, if thermal effects can be controlled.

The availability of a practical sensor for measuring supersaturation in fogs and clouds would permit us to try new approaches for solving current problems in cloud physics. For example, the parameterization of warm-cloud condensational growth in dynamic models could be explored using feedback between the models and a statistical description of microphysics, rather than using a computer-intensive approach including explicit microphysics; probability densities of RH measured by this sensor under various in-cloud conditions would be helpful here. In addition, K turbulence theory may require modification to deal adequately with microphysics in fogs and clouds; the nature and degree of complexity of the modification, in the direction of nonlocal turbulence closure, could be estimated by combining hygrometer and other microphysical measurements with modeling of specific fog and cloud cases. The sensor could be used in controlled laboratory experiments where mixing of saturated air is used to explore the basic nature of the turbulence mixing process, which requires better understanding and parameterization. Also, the sensor could be a key tool for understanding cloud-top interactions among radiation, entrainment, mixing, and microphysics.

Acknowledgments. This work was supported by Naval Ocean Systems Center, Code 54. Gar Lala of the State University of New York is thanked for providing the droplet size and temperature data for the two fogs. Appreciation is expressed to Roger Davies and Roddy Rogers of McGill University, Elaine Oran of Naval Research Laboratory, and Richard Flagan of California Institute of Technology for helpful discussions of fog and turbulence processes. Thank you and fond remembrances are for the late Jim Jiusto of SUNY, and Mike Corrin of Colorado State University.

APPENDIX A

Calibration of Saturation Hygrometer

1. Calibration for RH > 100%

Two independent means, one indirect and the other direct, are used to calibrate the hygrometer for RH > 100%; see Gerber (1980). The indirect means consists of measuring the temperature increase of the hygrometer mirror for given outputs of the infrared diode heaters, and relating these increases to the ambient supersaturation.

Gerber (1980) showed that the equation governing the size of the droplets on the hygrometer mirror was given by

$$S \approx \left[1 + \frac{L_h(T_r - T)}{R_v T^2}\right]\left[1 + \frac{A}{r_{100}} - \frac{Br_d^3}{r_{100}^3}\right] - 1 \quad (20)$$

when the ambient supersaturation S exceeded RH > 100%. The temperature of the droplets on the mirror is given by T_r, and the ambient temperature is T. The equilibrium droplet radius at RH = 100%, r_{100}, is used, because during operation of the hygrometer for RH > 100%, the infrared heaters are optically servoed to keep the droplets on the mirror at their r_{100} size as determined in the wet box. The droplets on the mirror, $r_{100} \sim 2.5$ μm, consist of diluted $(NH_4)_2SO_4$ solution, which permits Eq. (20) to be approximated by

$$S \approx \frac{L_h(T_r - T)}{R_v T^2} \qquad (21)$$

because neglecting the terms within the second brackets of Eq. (20) causes negligible error. Equation (21), an integral form of the Clausius–Clapeyron equation, shows that S is directly related to $T_r - T$ at a given value of T.

The calibration procedure is to establish in the laboratory the relationship between $T_r - T$ and the output of the infrared heaters, so that when the hygrometer is used in the field, the heater output can be related to S. The procedure for relating $T_r - T$ and heater output is done as follows. Two identical mirrors are placed in the radiation shield of the hygrometer (see Fig. 1). One is exposed to the infrared heaters, and the other is shielded from the heater radiation so that it remains at T. Both have miniature thermistors, which form two legs of a Wheatstone resistance bridge, imbedded in them. The hygrometer is placed in an isothermal chamber where the infrared heaters are turned on a known amount, and the bridge is balanced to determine the temperature difference between the two mirrors and $T_r - T$. This method does not require well-matched thermistors, yet is sensitive enough to detect the small temperature differences needed to infer S. For example, $T_r - T = 0.00174$°C corresponds to $S = 0.01\%$ and a resistance of 12 ohms to balance the bridge. This approach of determining S can be considered absolute because the temperature difference is based on known values of the thermistor temperature coefficient and this difference is related to S with a known relationship. Figure 14 shows an example of the indirect calibration method.

The direct method of calibrating the hygrometer for RH > 100% consists of exposing the hygrometer to the output of a continuous-flow thermal-gradient diffusion chamber. Figure 15 shows a schematic of this chamber in which air, prehumidified to RH ~ 100%, is accelerated to 1 m s^{-1} before being passed by the sensor. The top and bottom plates have wet inner surfaces, and are kept at different temperatures to produce supersaturations halfway between the plates as described by Fletcher (1966). Euler's equations for one-dimensional, irrotational, steady-state, compressible flow were solved for the chamber geometry, and indicated that the compression of the flow forced through the chamber corresponded to a temperature increase of 0.015°C near the chamber nozzle if molecular diffusion was ignored. While this increase is proportional to a reduction of $S \sim 1\%$, only a small fraction of this amount should be observed within the nozzle, because of the action of thermal molecular diffusion as the air passes through the chamber. However, just beyond the nozzle an increase in S comparable to $S \sim 1\%$ should be observed, because of the rapid pressure drop. Thus, the placement of the sensor with respect to the nozzle is critical. Figure 14 shows reasonable agreement between the direct and indirect calibrations of S. The tendency of the direct method to slightly overestimate S suggests that the sensor was not placed sufficiently far into the chamber nozzle.

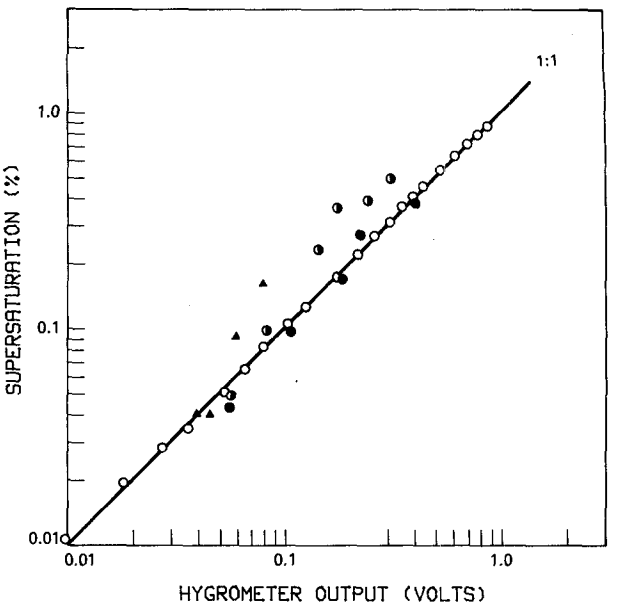

FIG. 14. Calibration results for the saturation hygrometer for RH > 100%. Open circles correspond to the indirect temperature measurement technique (open circles), and other data points are from the exposure of the hygrometer to the thermal-gradient diffusion chamber.

2. Calibration for RH = 100%

The proper operation of the hygrometer relies on a precise determination of its output at RH = 100% because this output determines whether the infrared heaters turn on to indicate supersaturation or remain off to indicate subsaturated conditions. To establish this output, the hygrometer is placed in a wet box with inner walls wetted with distilled water and outer walls covered with thick thermal insulation. In the wet box used here several hours are required to establish equilibrium conditions for the hygrometer. Successive exposures of the hygrometer in the wet box are highly reproducible (see Gerber 1980) and are a good indicator of the stability of the sensor while being used for atmospheric measurements.

This calibration must be considered nonabsolute because it is necessary to assume that, given sufficient time, the RH in the wet box will reach 100.00%. Measurements in fog support this assumption because the appearance of activated droplets closely coincides with a measured RH just in excess of 100.00%.

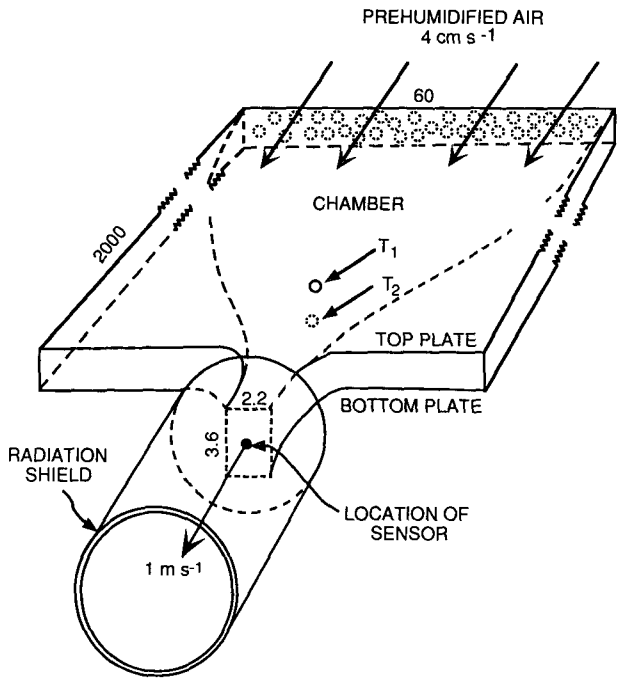

FIG. 15. Sketch of the continuous-flow thermal-gradient diffusion chamber used in the direct calibration of the saturation hygrometer for RH > 100%. Inner surfaces of plates are moistened with temperature T_1 of upper plate exceeding T_2 of lower plate; dimensions in cm.

3. Calibration for RH < 100%

For RH < 100%, the solution droplets on the hygrometer mirror shrink below their r_{100} size. A calibration curve for RH < 100% is established by relating the light scattered by the droplets to various values of known RH. This is done by placing the hygrometer into the wet box, which is assumed isothermal at a known temperature T_1, and at RH = 100.00%. Under those conditions the water vapor pressure $p(T_1)$ is known. The hygrometer is heated by a known amount to T_2, and the saturation water vapor pressure $p(T_2)$ is calculated from the Clausius–Clapeyron equation. For the droplets on the heated mirror, $p(T_1)$ appears less than the saturation vapor pressure at T_1, and in effect they scatter light as a function of RH = $p(T_1)/p(T_2)$. Figure 16 shows an example of a calibration curve for RH < 100%. The strong nonlinearity of the calibration curve seen near RH = 100% provides the sensitivity for the hygrometer for making accurate measurements near saturation.

APPENDIX B

Approximation of Droplet Growth Equation

Approximation formulas, summarized by Eq. (19), are derived to give an approximate fit to equilibrium and integral forms of the droplet growth equation (14). The formulas are given for some typical atmospheric nucleus types, consisting of sea-salt, urban, rural, soil (marine aerosol with Saharan dust), and $(NH_4)_2\,SO_4$ particles for which mean hygroscopic properties were determined by Hänel (1976) and Low (1969). The formulas are applied by specifying the type and radius r_d of the dry nucleus, the initial droplet radius r_0, a constant value of the ambient supersaturation S, and the time t over which the droplet is exposed to S.

The approximation formulas are partitioned in terms of S, the critical supersaturation S_c, and the critical radius r_c of the droplet. The latter two are properties of the Köhler curves (e.g., see Twomey 1977), which are solutions of the droplet growth equation under equilibrium conditions where $dr/dt = 0$ and the equilibrium supersaturation S_e at the surface of the droplets is given to a good approximation by

$$S_e = \frac{A}{r} - \frac{Br_d^3}{r^3}. \tag{22}$$

Combining Eqs. (14) and (22) gives

$$r\frac{dr}{dt} = C(S - S_e). \tag{23}$$

Figure 17 illustrates a Köhler curve and the relationship between S_e, S_c, r_c, and r_{100} for droplets containing the same nucleus.

1. Haze droplets: $r_0 \leq r_c$; $-1 < S \leq 0$ [B.1]

Given the large growth rate of these small droplets, the assumption is made that they quickly reach equilibrium with S so that $dr/dt = 0$ and the haze equation

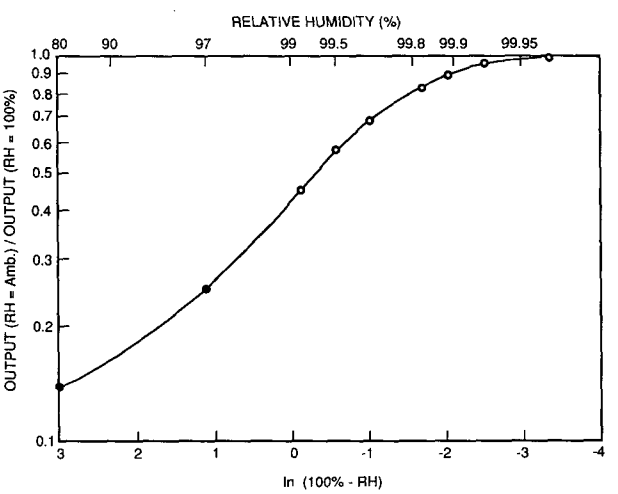

FIG. 16. Saturation hygrometer calibration for RH < 100%. Hygrometer's optical output is normalized by its output at RH = 100% and is shown as a function of measured values (open circles) and estimated values (solid circles).

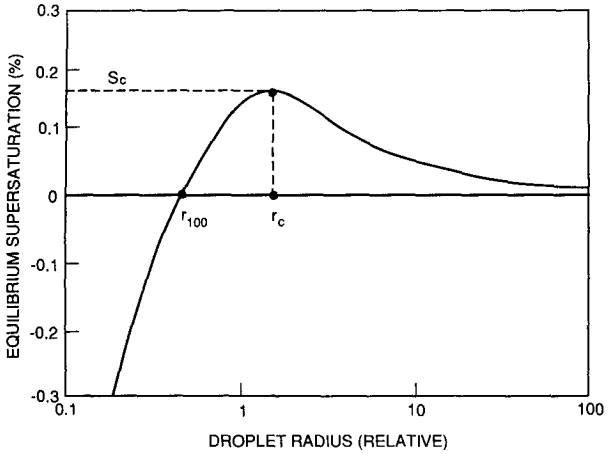

FIG. 17. Sketch of Köhler curve for droplets containing an equal amount of hygroscopic material, showing the relationship between equilibrium supersaturation S_e, S_c, r_c, and r_{100}.

$$S_e = \frac{\exp[(2\sigma')/(r\rho_w R_v T)]}{1 + \bar{\mu} m_d/m_w} - 1 \qquad (24)$$

based on a derivation by Fitzgerald (1975), applies. Hänel (1976) gives the expression for the droplet surface tension σ' and tabulates mean measured values of the linear mass increase coefficient $\bar{\mu}$ for the different atmospheric nucleus types. Low (1969) gives $\bar{\mu}$ for $(NH_4)_2\,SO_4$ nuclei. The mass of water in the droplet is m_w, m_d is the nucleus mass, ρ_w is the density of water, and R_v is the specific gas constant for water vapor.

Equation (24), as well as other haze equations given by Kasten (1969), Barnhart and Streete (1970), Hänel (1976), and Wells et al. (1977), have in common that they cannot be solved directly for r, and that the approximations to these equations either lose accuracy for haze droplets smaller than $r = 0.1$ μm, or have no solution at RH = 100%.

Gerber (1985) describes an approximate solution to Eq. (24) explicit in r given by

$$r = \left[\frac{C1 r_d^{C2}}{C3 r_d^{C4} - \log(S+1)} + r_d^3\right]^{1/3}, \qquad (25)$$

where the constants $C1$, $C2$, $C3$, $C4$ are listed in Table 1 for the various nucleus types; Eq. (25) does not include the hysteresis effect, and the results are given for increasing humidity. The form of Eq. (25) is the same as the approximate solution of Eq. (24) given by Fitzgerald (1975), except for the term $C3 r_d^{C4}$, which includes the influence of the Kelvin effect. This term enables Eq. (25) to be applied to particles as small as 0.01 μm, and to give a solution at RH = 100%. The behavior of Eqs. (24) and (25) are compared for $(NH_4)_2\,SO_4$ nuclei in Fig. 18. The mean relative difference between approximate and exact solutions of Eq. (24) is 3% for $S + 1 > 0.75$.

TABLE 1. Constants used with approximate droplet growth equations for various types of aerosol particles.

	Particle type				
	C1	*C2*	*C3*	*C4*	*B*
Sea salt	0.7674	3.079	2.572E−11	−1.424	1.02
Urban	0.3926	3.101	4.190E−11	−1.404	0.450
Rural	0.2789	3.115	5.415E−11	−1.399	0.280
Soil	0.0533	3.005	1.805E−11	−1.590	0.115
$(NH_4)_2SO_4$	0.4809	3.082	3.110E−11	−1.428	0.600

2. Haze droplets: $r_0 \leq r_c$; $0 < S \leq S_c$ [B.2]

For this range of r_0 and S, it is again assumed that $dr/dt = 0$, and that the Köhler curves can be approximated with a straight line between r_{100} and r_c:

$$r = r_c\left[0.423\left(\frac{S}{S_c} - 1\right) + 1\right], \qquad (26)$$

where

$$r_c = \left(\frac{3Br_d^3}{A}\right)^{1/2}; \quad S_c = \frac{2A}{3r_c} \qquad (27)$$

and the values of B, given in Table 1, depend on nucleus type; $A = 1.3 \times 10^{-7}$ cm.

3. Activated droplets: $r_0 \leq r_c$; $S > S_c$ [B.3]

For this case an approximate expression is obtained for r versus t by integrating Eq. (23) with the assumption that S_e is a constant:

$$r = [2C(S - S_e)^{K1} t + r_0^2]^{1/2}, \qquad (28)$$

where

$$K1 = \left(1 - 0.05\,\frac{S_e}{S}\right)^2 \qquad (29)$$

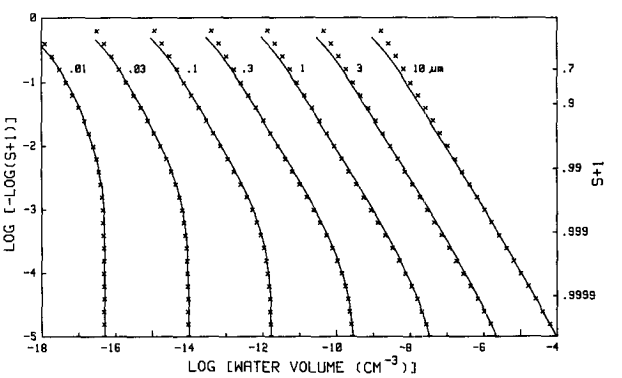

FIG. 18. Volume of droplets formed on $(NH_4)_2\,SO_4$ nuclei of indicated radii as a function of saturation ratio $S + 1$; solid curves are exact solutions [Eq. (24)], and crosses (×) are predictions of approximate haze equation [Eq. (25)].

is an empirically derived correction factor to compensate in part for errors generated by this assumption. Equation (28) and (29) use $S_e = S_c$ and $r_0 = r_c$ because droplets find themselves at r_c without any time having elapsed according to the conditions specified in section B.2.

4. Activated droplets: $r_0 > r_c$; $S > S_e$ [B.4]

The approximate growth equation is given by Eq. (28) with

$$S_e = \frac{A}{r_0} - \frac{Br_d^3}{r_0^3}. \tag{30}$$

5. Activated droplets: $r_0 > r_c$; $S < S_e$ [B.5]

For this case, Eq. (23) is solved for r as in B.3 to yield

$$r = [-2C(S_e - S)^{K2}t + r_0^2]^{1/2}, \tag{31}$$

where the correction factor is given by

$$K2 = \left[1 - 0.03\left(\frac{S_e}{2S_e - S}\right)\right]^2 \tag{32}$$

and S_e is given by Eq. (30).

Given that droplets evaporate when $S < S_e$, Eq. (31) will cause droplets to shrink to r_c, given large enough t. Beyond that time, the size of the droplets rapidly decreases and is described in B.1 and B.2. A critical time t_c is defined equal to the time required for the droplets to evaporate from r_0 to r_c; t_c is found by solving Eq. (31) for time:

$$t_c = \frac{r_0^2 - r_c^2}{2C(S_e - S)^{K2}}. \tag{33}$$

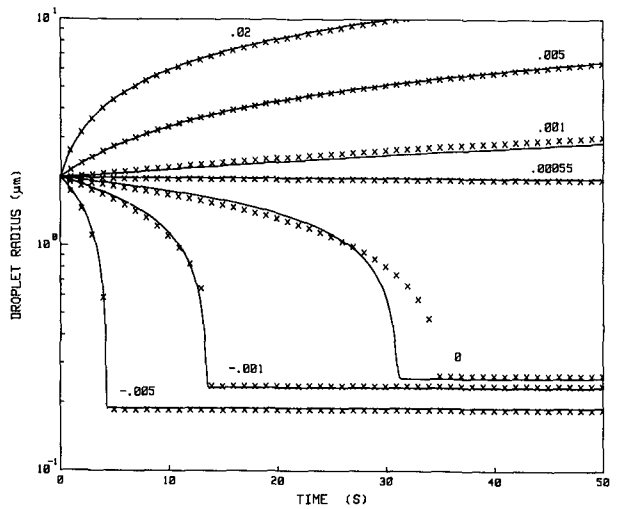

FIG. 19. Growth of a solution droplet with initial radius $r_0 = 2.5$ μm, formed on a $(NH_4)_2SO_4$ dry nucleus with $r_d = 0.05$ μm, according to the droplet growth equation [solid curves; Eq. (14)] and the approximation formulas [crosses, ×, Eq. (19)] for the indicated values of ambient supersaturation.

If $t < t_c$, Eq. (31) determines r. If $t \geq t_c$, Eq. (26) gives r when $0 < S \leq S_c$, and Eq. (25) gives r when $S \leq 0$. In all cases, when $S = S_e$, $r = r_0$.

6. Summary

Equation (19) is composed of the basic set of approximation formulas given by Eqs. (25), (26), (28), and (31). Figure 19 compares solutions of Eq. (19) with the numerical solution of the droplet growth equation [Eq. (14)] for a $(NH_4)_2SO_4$ nuclei exposed to different humidities. The approximate solutions differ somewhat from those of Eq. (14), especially near RH = 100%. These differences, as well as the approximations inherent in the present simple approach to droplet growth, should cause less error in microphysical calculations than errors caused by uncertainties in modeling droplet growth in turbulent mixing.

REFERENCES

Albrecht, B. A., D. A. Randall, and S. Nicholls, 1988: Observations of marine stratocumulus clouds during FIRE. *Bull. Amer. Meteor. Soc.*, **69**, 618–626.

Alves, A. R., 1987: On the interactions of longwave radiation, microphysics, and turbulence in boundary layer clouds. Ph.D thesis, Purdue University, 184 pp.

Aranson, G., and P. S. Brown, 1971: Growth of cloud droplets by condensation: A problem in computational stability. *J. Atmos. Sci.*, **28**, 72–77.

Baker, M. B., and J. Latham, 1979: The evolution of droplet spectra and the rate of production of embryonic raindrops in small cumulus clouds. *J. Atmos. Sci.*, **36**, 1612–1615.

——, R. E. Breidenthal, T. W. Choularton, and J. Latham, 1984: The effects of turbulent mixing in clouds. *J. Atmos. Sci.*, **41**, 299–304.

Barnhardt, E. A., and J. L. Streete, 1970: A method for predicting atmospheric aerosol scattering coefficients in the infrared. *Appl. Opt.*, **9**, 1337–1344.

Bott, A., U. Sievers, and W. Zdunkowski, 1990: A radiation fog model with a detailed treatment of the interaction between radiative transfer and fog microphysics. *J. Atmos. Sci.*, **47**, 2153–2166.

Bower, K. N., and T. W. Choularton, 1988: The effects of entrainment on the growth of droplets in continental cumulus clouds. *Quart. J. Roy. Meteor. Soc.*, **114**, 1411–1434.

Broadwell, J. E., and R. E. Breidenthal, 1982: A simple model of mixing and chemical reaction in a turbulent shear layer. *J. Fluid Mech.*, **125**, 397–410.

——, and M. B. Mungal, 1988: Molecular mixing and chemical reactions in turbulent shear layers. Preprints, *22nd Int. Combustion Symp.*, Seattle, 18 pp. [Available from the Combustion Institute, Pittsburgh, PA.]

Brown, R., 1980: A numerical study of radiation fog with an explicit formulation of the microphysics. *Quart. J. Roy. Meteor. Soc.*, **106**, 781–802.

Choularton, T. W., G. Fullerton, J. Latham, C. S. Mills, M. H. Smith, and I. M. Stromberg, 1981: A field study of radiation fog in Meppen, West Germany. *Quart. J. Roy. Meteor. Soc.*, **107**, 381–394.

Clark, T. L., and W. D. Hall, 1979: A numerical experiment on stochastic condensation theory. *J. Atmos. Sci.*, **36**, 470–483.

Cooper, W. A., 1989: Effects of variable droplet growth histories on droplet size distributions. Part I: Theory. *J. Atmos. Sci.*, **46**, 1301–1311.

Corrsin, S., 1974: Limitations of gradient transport models in random

walks and in turbulence. *Advances in Geophysics, No. 18A,* Academic Press, p. 25.

Davies, D. K., 1963: The incipient condensation of water vapour on a gold surface. *Brit. J. Appl. Phys.,* **14,** 567–571.

Davies, R., 1985: Response of cloud supersaturation to radiative forcing. *J. Atmos. Sci.,* **42,** 2820–2825.

——, and A. R. Alves, 1989: Flux divergence of thermal radiation within stratiform clouds. *J. Geophys. Res.,* **94,** 16 277–16 286.

Fitzgerald, J. W., 1975: Approximation formulas for the equilibrium size of an aerosol particle as a function of dry size and composition and the ambient relative humidity. *J. Appl. Meteor.,* **14,** 1044–1049.

——, 1978: A numerical model of the formation of droplet spectra in advection fogs at sea and its applicability to fogs off Nova Scotia. *J. Atmos. Sci.,* **35,** 1522–1535.

Fitzjarrald, D. R., and G. G. Lala, 1989: Hudson Valley fog environments. *J. Appl. Meteor.,* **28,** 1303–1328.

Fletcher, N. H., 1966: *The Physics of Rainclouds.* Cambridge University Press, 390 pp.

Gerber, H. E., 1980: A saturation hygrometer for the measurement of relative humidity between 95% and 105%. *J. Appl. Meteor.,* **19,** 1196–1208.

——, 1981: Microstructure of a radiation fog. *J. Atmos. Sci.,* **38,** 454–458.

——, 1985: Relative-humidity parameterization of the Navy aerosol model (NAM). NRL Rep. 8956. Naval Research Laboratory, Washington, D.C., 13 pp.

Hasegawa, S., and J. W. Little, 1977: The NBS two-pressure humidity generator, Mark 2. *J. Res. Nat. Bur. Stand.,* **81A,** 81–88.

Hänel, G., 1976: Properties of atmospheric aerosol particles as functions of the relative humidity at thermodynamic equilibrium with the surrounding moist air. *Advances in Geophysics,* Vol. 19, Academic Press, 73–188.

——, 1987: The role of aerosol properties during the condensational stage of cloud: A reinvestigation of numerics and microphysics. *Beitr. Phys. Atmos.,* **60,** 321–337.

Howell, W. E., 1949: The growth of cloud drops in uniformly cooled air. *J. Meteor.,* **6,** 134–149.

Hudson, J. G., 1980: Relationship between fog condensation nuclei and fog microstructure. *J. Atmos. Sci.,* **37,** 1854–1867.

James, J. E., H. Gerber, and S. G. Gathman, 1989: Navy tethered balloon measurements made during the "FIRE" marine stratocu IFO, July 1987. NRL Memo Rep. 6445, Naval Research Laboratory, Washington, D.C., 122 pp.

Jensen, J. B., and M. B. Baker, 1989: A simple model of spectral evolution during turbulent mixing. *J. Atmos. Sci.,* **46,** 2812–2829.

Jiusto, J. E., and G. G. Lala, 1983: The Fog Project—1982. *Proc. of Ninth Conf. on Aerospace and Aeronautical Meteorology,* Omaha, Amer. Meteor. Soc., 95–98.

Jonas, P. R., and B. J. Mason, 1982: Entrainment and the droplet spectrum in cumulus clouds. *Quart. J. Roy. Meteor. Soc.,* **108,** 857–869.

Kasten, F., 1969: Visibility forecast in the phase of precondensation. *Tellus,* **21,** 631–635.

Low, R. D. H., 1969: A theoretical study of nineteen condensation nuclei. *J. Rech. Atmos.,* **4,** 65–78.

Manton, M. J., 1979: On the broadening of a droplet distribution by turbulence near cloud base. *Quart. J. Roy. Meteor. Soc.,* **105,** 899–914.

Meyer, M. B., and G. G. Lala, 1990: Climatological aspects of radiation fog occurrence at Albany, New York. *J. Climate,* **3,** 577–586.

——, ——, and J. E. Jiusto, 1986: FOG-82: A cooperative field study of radiation fog. *Bull. Amer. Meteor. Soc.,* **67,** 825–832.

——, J. E. Jiusto, and G. G. Lala, 1980: Measurements of visual range and radiation-fog (haze) microphysics. *J. Atmos. Sci.,* **37,** 622–629.

Nelson, D. E., and E. J. Amdur, 1965: The mode of operation of saturation temperature hygrometers based on electrical detection of salt-solution phase transition. *Humidity and Moisture, Vol. 1,* R. E. Ruskin, Ed., Reinhold, 617–626.

Paluch, I. G., and D. G. Baumgardner, 1989: Entrainment and fine-scale mixing in a continental convective cloud. *J. Atmos. Sci.,* **46,** 261–278.

Paluch, I. R., and C. A. Knight, 1986: Does mixing promote cloud droplet growth. *J. Atmos. Sci.,* **43,** 1994–1998.

Pinnick, R. G., D. L. Hoihjelle, G. Fernandez, E. B. Stenmark, J. D. Lindberg, G. B. Hoidale, and S. G. Jennings, 1978: Vertical structure in atmospheric fog and haze and its effects on visible and infrared extinction. *J. Atmos. Sci.,* **35,** 2020–2032.

Pope, S. B., 1988: The evolution of surfaces in turbulence. *Int. J. Eng. Sci.,* **26,** 445–469.

Pruppacher, H. R., and J. D. Klett, 1978: *Microphysics of Clouds and Precipitation.* Reidel, 714 pp.

Roach, W. T., 1976: On the effect of radiative exchange on the growth by condensation of a cloud or fog droplet. *Quart. J. Roy. Meteor. Soc.,* **102,** 361–372.

Rodhe, B., 1962: The effect of turbulence on fog formation. *Tellus,* **14,** 49–86.

Saxena, V. K., and N. Fukuta, 1982: The supersaturation in fogs. *J. Rech. Atmos.,* **16,** 327–335.

Squires, P., 1952: The growth of cloud drops by condensation. *Aust. J. Res.,* **A5,** 59–86.

Stull, R. B., 1984: Transilient turbulence theory. Part I: The concept of eddy-mixing across finite distances. *J. Atmos. Sci.,* **41,** 3351–3367.

Telford, J. W., and S. K. Chai, 1980: A new aspect of condensation theory. *Pure Appl. Geophys.,* **118,** 720–742.

——, and P. B. Wagner, 1981: Observations of condensation growth determined by entity type mixing. *Pure Appl. Geophys.,* **119,** 934–965.

Turton, J. D., and R. Brown, 1987: A comparison of a numerical model of radiation fog with detailed observations. *Quart. J. Roy. Meteor. Soc.,* **113,** 37–54.

Twomey, S., 1977: *Atmospheric Aerosols.* Elsevier, 302 pp.

——, 1986: Comments on "Interactions among turbulence, radiation, and microphysics in Arctic stratus clouds." *J. Atmos. Sci.,* **43,** 2752.

Warner, J., 1968: The supersaturation in natural clouds. *J. Rech. Atmos.,* **3,** 233–237.

Welch, R. M., M. G. Ravichandran, and S. K. Cox, 1986: Prediction of quasi-periodic oscillation in radiation fogs. Part I: Comparison of simple similarity approaches. *J. Atmos. Sci.,* **43,** 633–651.

Wells, W. C., G. Gal, and M. W. Munn, 1977: Aerosol distribution in maritime air and predicted scattering coefficient in the infrared. *Appl. Opt.,* **16,** 654–659.

Wylie, R. G., D. K. Davies, and C. A. Caw, 1965: The basic process of the dew-point hygrometer. *Humidity and Moisture, Vol. 1,* R. E. Ruskin, Ed., Reinhold, 125–134.